Chemical Science

ROYAL SOCIETY OF CHEMISTRY

EDGE ARTICLE

View Article Online
View Journal | View Issue



Cite this: *Chem. Sci.*, 2026, **17**, 8272

All publication charges for this article have been paid for by the Royal Society of Chemistry

# Coaxial 3D printing of zeolite core–shell structured catalysts for integrated $NO_x$ adsorption and selective catalytic reduction in cold start application

Yingzhen Wei,†[a] Jingyi Feng,†[ab] Dan Li,[a] Youji Qi,[a] Mengyang Chen,[c] Shuang Wang,[d] Jinfeng Han[ab] and Jihong Yu *[ab]

Received 18th November 2025
Accepted 26th February 2026

DOI: 10.1039/d5sc08988c

rsc.li/chemical-science

$NH_3$ selective catalytic reduction ($NH_3$-SCR) is the most effective technology to alleviate $NO_x$ emission from diesel vehicles but faces the cold start problem. Ideally, integrating passive $NO_x$ adsorption (PNA) and $NH_3$-SCR could achieve a cost-effective and space-friendly tandem of these two units, but designing effective catalysts to achieve both high adsorption capacity and superior catalytic activity remains a challenge. Herein, we have successfully developed an integrated PNA-SCR catalyst system based on the Pd-SSZ-13@Cu-SSZ-13 core–shell structured zeolite composite *via* coaxial 3D printing, which affords ultra-high $NO_x$ removal efficiency (96%) over the entire PNA and $NH_3$-SCR process. Over the core–shell structure with spatially confined effects, $NO_x$ can be effectively adsorbed in the Pd-SSZ-13 core at low temperature (<170 °C) with less $H_2O$ competition, which is subsequently released at 200–350 °C to react completely with $NH_3$ over the Cu-SSZ-13 shell without excessive side reactions. Based on the optimal component of composite catalysts, Pd-SSZ-13@Cu-SSZ-13 displays high adsorption capacity ($NO_x$/Pd = 0.54), high adsorption rate, optimized desorption temperature (~250 °C), and excellent $NH_3$-SCR activity, providing a potential solution to the cold start challenge in $NO_x$ elimination.

## Introduction

The abatement of $NO_x$ emissions from diesel engine exhaust represents an imperative challenge, holding profound implications for environmental sustainability and public health. To this end, Cu-exchanged zeolites with small-pore structures have been rapidly developed for selective catalytic reduction of $NO_x$ with ammonia ($NH_3$-SCR) and have made tremendous progress in the past decade.[1–5] As the predominant catalyst, Cu-exchanged SSZ-13 zeolite (Cu-SSZ-13, CHA) has been successfully commercialized owing to its excellent hydrothermal stability and catalytic activity, which can achieve 100% $NO_x$ conversion at temperatures above 200 °C.[6–9] However, the $NO_x$ emission during the cold start remains an essential challenge due to the insufficient low-temperature activity of $NH_3$-SCR catalysts.[10,11] An appealing strategy is introducing passive $NO_x$ adsorbers (PNAs) into exhaust-treatment systems to handle the cold start problem.[12,13] Over PNA units, $NO_x$ can be trapped at low temperature (<170 °C) and released at the operating temperature of the $NH_3$-SCR catalyst (200–350 °C).[14–16] Currently, zeolite-supported Pd catalysts (*e.g.*, Pd-SSZ-13) are the extensively studied PNA materials, which attract significant attention because of their superb $NO_x$ adsorption efficiency and capacity.[17–20]

To avoid undesired oxidation of $NH_3$ by precious metals, the PNA unit should be located ahead of the ammonia dosing point, upstream of the SCR catalysts.[21,22] However, the introduction of an additional unit leads to a more complicated post-treatment system and higher cost. Selleri *et al.* proposed the "AdSCR" concept based on non-precious metal $NO_x$ adsorbers and SCR catalysts, which exhibited excellent $NO_x$ removal performance during the cold start.[23–25] However, the "AdSCR" concept has been rarely investigated with the presence of $H_2O$, which can seriously affect the adsorption behaviors of vehicle exhaust treatment catalysts. Creating tandem catalysts with Pd-based adsorbents and $NH_3$-SCR catalysts can maintain adsorption and catalytic activity under humid conditions while avoiding the introduction of additional components. To this end, the Olsson group demonstrated a dual-layer monolith catalyst (Pd/

[a]*State Key Laboratory of Inorganic Synthesis and Preparative Chemistry, College of Chemistry, Jilin University, 2699 Qianjin Street, Changchun 130012, P. R. China. E-mail: jihong@jlu.edu.cn*

[b]*International Centre of Future Science, Jilin University, 2699 Qianjin Street, Changchun 130012, P. R. China*

[c]*School of Pharmaceutical and Chemical Engineering, Taizhou University, Taizhou 317000, P. R. China*

[d]*Henan Province Function-Oriented Porous Materials Key Laboratory, College of Chemistry and Chemical Engineering, Luoyang Normal University, Luoyang 471934, P. R. China*

† These authors contributed equally to this work.

SSZ-13 + Cu/SSZ-13) coated on cordierite for $NO_x$ abatement, which showed favorable coupled effects. However, this method still suffers from $NO_x$ storage losses due to the low loading of Pd-SSZ-13 and inhibited high-temperature catalytic conversion caused by the side reaction of non-selective ammonia oxidation occurred in precious metal Pd.[26] Therefore, it is of great significance to develop facile strategies for effectively integrating PNA and SCR catalysts to overcome the above-mentioned issues, and thus improve the PNA-SCR technology.

As an emerging technology, 3D printing presents significant advantages in efficient and accurate construction of zeolite monolithic catalysts with high zeolite loading and desirable configurations, enabling accelerated heat and mass transfer.[27–33] A series of zeolite monoliths such as ZSM-5, NaX, and SAPO-34 have been fabricated *via* 3D printing, which displayed outstanding adsorption, separation, and catalytic performance.[34–37] Recently, our group developed a zeolite-based coaxial 3D printing technology that enables the general creation of core–shell structured catalysts with a variety of capabilities. Simultaneously, the thickness of the core/shell layers can be flexibly regulated to meet specific functional requirements.[38] Employing coaxial 3D printing technology, PNA materials can be controllably integrated with $NH_3$-SCR components to construct PNA-SCR core–shell monolithic catalysts for efficient coupling of low-temperature adsorption and high-temperature catalysis. The unique core–shell structure with spatially confined effects is expected to arrange adsorption and catalytic processes in a favorable order and suppress side reactions of ammonia oxidation. Meanwhile, the high zeolite loading and hierarchical structure are conducive to great adsorption capacity and rapid transfer rate. Therefore, we believe that coaxial 3D printing technology is a promising approach for flexibly constructing PNA-SCR coupled core–shell structured catalysts to maximize the effect of coupling while addressing the challenges of $NO_x$ storage losses and suppressed $NH_3$-SCR activity.

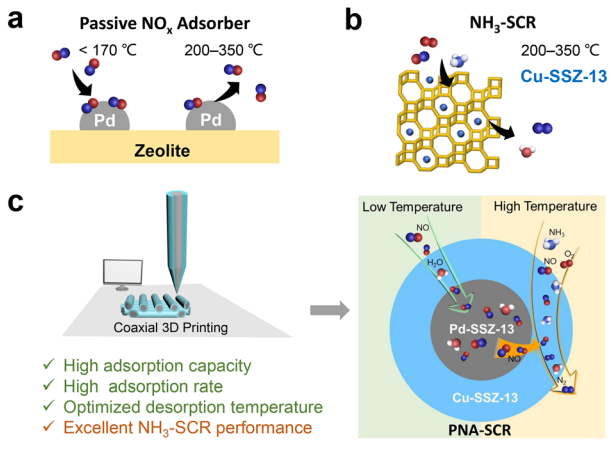


Fig. 1 Schematic diagram of the passive $NO_x$ adsorber (a) and $NH_3$-SCR catalyst (b). (c) Diagrammatic drawing of the design and fabrication of 3D-printed Pd-SSZ-13@Cu-SSZ-13 core–shell structured catalysts for efficient tandem of low-temperature $NO_x$ adsorption and high-temperature catalysis.

In this work, an integrated PNA-SCR catalyst with Pd-SSZ-13 as the core and Cu-SSZ-13 as the shell has been successfully constructed *via* coaxial 3D printing (Fig. 1). The Pd-SSZ-13 in the core layer can capture $NO_x$ at <170 °C and desorb it as the temperature increases to 200–350 °C (Fig. 1a–c). The released $NO_x$ from the core layer diffuses to the Cu-SSZ-13 shell and launches an effective SCR reaction with $NH_3$ at operating temperature (Fig. 1b and c). With the design of the core–shell structure, the Pd-SSZ-13@Cu-SSZ-13 catalyst exhibits high adsorption capacity ($NO_x$/Pd = 0.54), high adsorption rate, optimized desorption temperature, as well as excellent $NH_3$-SCR activity with suppressed ammonia oxidation, thus achieving an outstanding PNA-SCR coupled performance (Fig. 1c). This work provides a powerful strategy for the treatment of $NO_x$ emissions during the cold start of vehicles.

## Results and discussion

### Fabrication and characterization of integrated catalysts

Pd-SSZ-13@Cu-SSZ-13 core–shell structured catalysts were fabricated by coaxial 3D printing. Commercial Cu-SSZ-13 (Si/Al = 4.6, Fig. S1) was thoroughly mixed with an inorganic binder (halloysite nanotubes, HNTs, Fig. S2), an organic binder (hydroxypropyl methylcellulose, HPMC), and solvents (deionized water and ethanol) to obtain printing ink of the shell layer with suitable rheology (Fig. S3a and b). The printing ink of the core layer was prepared by mixing $Pd(NO_3)_2$ solution, $NH_4$-SSZ-13 zeolites (Si/Al = 11, Fig. S4), and binders to generate suitable rheological behaviors (Fig. S3a–c). The Pd-SSZ-13@Cu-SSZ-13 monoliths were coaxially 3D printed using a customized coaxial nuzzle (20 G/16 G). Catalysts with different core–shell ratios were fabricated by regulating the extruding pressure. The pristine monoliths were dried at room temperature overnight and then calcined at 600 °C for 5 h to remove the organic binder. The prepared core–shell structured catalysts were donated as 3D-PdZ@CuZ. For comparison, Cu-SSZ-13 and Pd-SSZ-13 monoliths were also 3D printed, named 3D-CuZ and 3D-PdZ. According to inductively coupled plasma optical emission spectroscopy (ICP-OES) measurement (Table S1), the Pd and Cu loadings in 3D-PdZ and 3D-CuZ monoliths are 0.70 wt% and 4.10 wt%, respectively.

By a coaxial 3D printing strategy, 3D-PdZ@CuZ zeolite monoliths with different sizes and geometric patterns were successfully fabricated (Fig. 2a). Honeycomb structured 3D-PdZ, 3D-CuZ, and 3D-PdZ@CuZ catalysts with inter-connected channels are illustrated in Fig. 2b. As observed from the top views of the scanning electron microscope (SEM) images (Fig. 2c), the crossing rods of the monolith possess a uniform size of about 800 μm. Fig. 2d–f illustrates cross-sectional SEM images of the representative catalyst at different magnifications, from which an integrated and uniform core–shell structure can be recognized. Zeolite particles in the core and shell layers are bonded by HNTs to form a monolith, as shown in Fig. 2f. SEM elemental mapping was performed to investigate the metal distribution in the cross-section of the catalyst (Fig. 2g). Pd and Cu elements are distributed in the core layer and shell layer, respectively, further confirming the successful

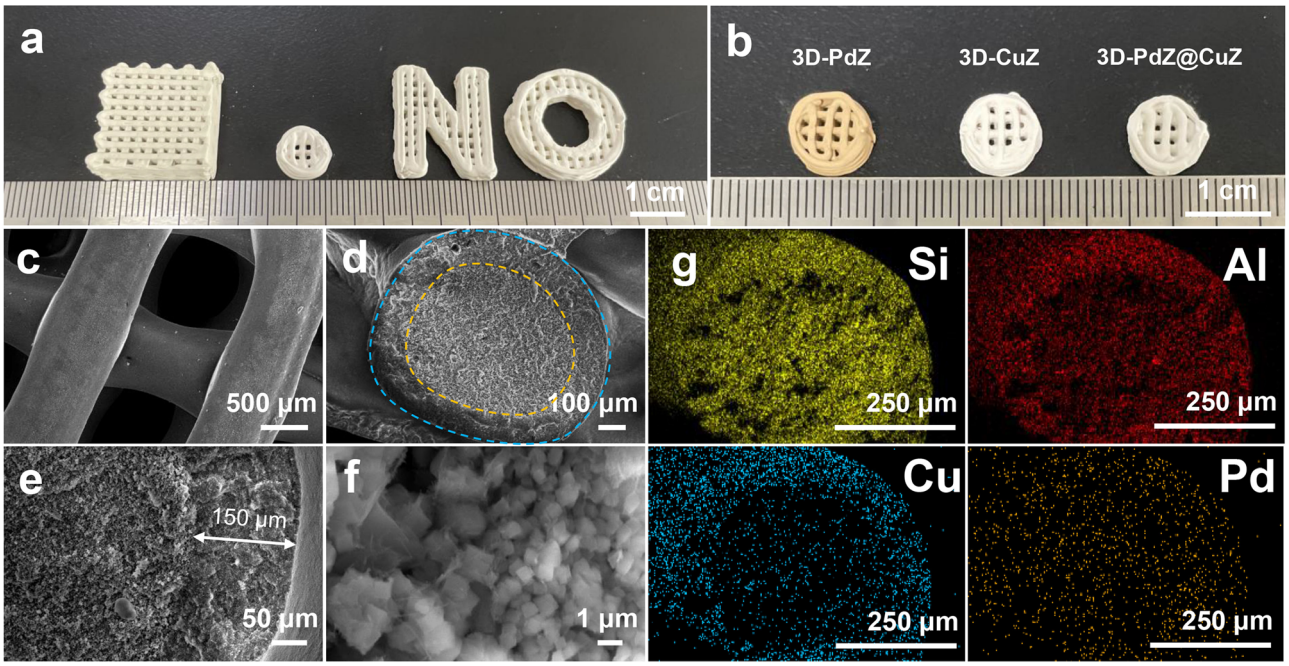


Fig. 2 (a) Digital photographs of 3D-PdZ@CuZ monoliths with different structures. (b) Digital photographs of 3D-PdZ, 3D-CuZ, and 3D-PdZ@CuZ catalysts. SEM images of 3D-PdZ@CuZ from top view (c) and cross-sectional view (d–f) at different magnifications. (g) Scanning electron microscopy energy dispersive X-ray spectroscopy (SEM-EDS) elemental mapping images of a representative cross-sectional 3D-PdZ@CuZ monolith (yellow: Si, red: Al, blue: Cu, and orange: Pd).

construction of the Pd-SSZ-13@Cu-SSZ-13 monolithic core–shell structured catalyst. The denser distribution of Al in the shell also suggests that Cu-SSZ-13 zeolites with lower Si/Al are distributed in the shell layer.

$N_2$ adsorption–desorption (Fig. S5 and Table S2) characterization displays similar isotherms and pore structure data over 3D-CuZ, 3D-PdZ, and 3D-PdZ@CuZ. As evidenced by SEM images (Fig. 2b–f) and pore size distributions (Fig. S5b), 3D printed core–shell catalysts feature hierarchical architectures, combining the inherent micropore structure of the zeolites, meso/macropores from the bonding/accumulation of zeolite crystals and inorganic binders, and the 3D-interconnected honeycomb structure channels. This hierarchical structure enables the free diffusion of NO (kinetic diameter 0.317 nm) and $NH_3$ (kinetic diameter 0.260 nm) through the shell and reach the core under reaction conditions. The X-ray diffraction (XRD) patterns of the 3D-CuZ, 3D-PdZ, and 3D-PdZ@CuZ catalysts are presented in Fig. S6. The characteristic diffraction peaks of the CHA zeolite structure are observed on all catalysts, indicating that the zeolite framework structure is well preserved during the process of coaxial 3D printing. X-ray photoelectron spectroscopy (XPS, Fig. S7) and temperature-programmed reduction of hydrogen ($H_2$-TPR, Fig. S8) patterns also show negligible changes of active Cu and Pd species between 3D-CuZ/3D-PdZ and 3D-PdZ@CuZ. These results demonstrate that the original physicochemical properties and the active species of the adsorbent and catalyst can be well maintained during the construction of core–shell structured catalysts by coaxial 3D printing.

### Core–shell ratio control of integrated catalysts

To investigate the optimal core–shell ratio in PNA-SCR performance, the monolithic catalysts with different core and shell thicknesses were constructed *via* coaxial 3D printing under different extruding pressures. Fig. 3a–e displays the cross-sectional SEM images of catalysts, 3D-PdZ, 3D-PdZ(66%)@CuZ (including 66% core layer and 34% shell layer), 3D-PdZ(45%)@CuZ (including 45% core layer and 55% shell layer), 3D-PdZ(26%)@CuZ (including 26% core layer and 74% shell layer), and 3D-CuZ, respectively. The percentages of the core and shell layers were calculated from ICP-OES results (Table S1).

$NO_x$ storage and release curves were obtained to evaluate the PNA performance. As depicted in Fig. 3f, all samples capture $NO_x$ rapidly when the feed is switched to the catalysts, resulting in a dramatic decrease in $NO_x$ concentrations at 100 °C. After reaching the minimum value, the $NO_x$ concentrations gradually reapproach the initial values. Subsequently, as the temperature increases, a second decrease in $NO_x$ concentrations appears at ~150 °C, which is mainly attributed to the desorption of $H_2O$, releasing available Pd sites for $NO_x$ adsorption. Eventually, the $NO_x$ outlet concentrations exceed the initial concentration, indicating the desorption of $NO_x$ at high temperature. The amounts of $NO_x$ adsorption and $NO_x$/Pd ratio are calculated and displayed in Fig. 3g. The adsorption capacities of the core–shell structured catalysts decrease with decreasing core thickness, which is associated with the reduced proportion of Pd-SSZ-13. It is worth noting that the $NO_x$/Pd ratios of the core–shell structured catalysts are unexpectedly enhanced at lower Pd-SSZ-13 loadings, which demonstrates that more $NO_x$ can be adsorbed

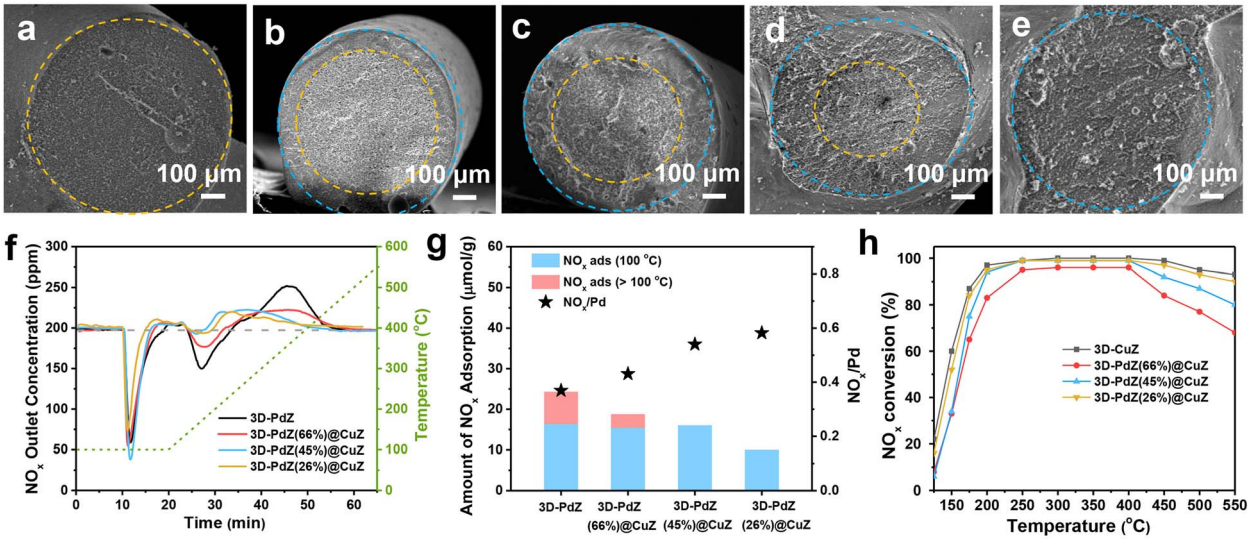


Fig. 3 The cross-sectional SEM images of 3D-PdZ (a), 3D-PdZ(66%)@CuZ (b), 3D-PdZ(45%)@CuZ (c), 3D-PdZ(26%)@CuZ (d), and 3D-CuZ (e). PNA performance (f), amount of $NO_x$ adsorption and corresponding $NO_x$/Pd (g) of 3D-PdZ, 3D-PdZ(66%)@CuZ, 3D-PdZ(45%)@CuZ, and 3D-PdZ(26%)@CuZ. (h) $NH_3$-SCR performance of 3D-CuZ, 3D-PdZ(66%)@CuZ, 3D-PdZ(45%)@CuZ, and 3D-PdZ(26%)@CuZ. (PNA reaction conditions: [NO] = 200 ppm, $[O_2]$ = 10%, $[H_2O]$ = 5%, and balanced with $N_2$. $NH_3$-SCR reaction conditions: [NO] = $[NH_3]$ = 500 ppm, $[O_2]$ = 5%, $[H_2O]$ = 5%, balanced with $N_2$, 0.24 g monolith sample, and WHSV = 50 000 $cm^3\ g^{-1}\ h^{-1}$).

per Pd site on average, resulting in higher utilization of the precious metal Pd (Fig. S9).

The $NH_3$-SCR tests were performed with the same weight of monolithic samples (WHSV = 50 000 $cm^3\ g^{-1}\ h^{-1}$). As presented in Fig. 3h, increasing the proportion of the core layer leads to a gradual decline in catalytic conversion at low (<200 °C) and high (>400 °C) temperatures over catalysts, owing to the reduced loading of Cu-SSZ-13. As the percentage of the core increases to 66%, there is a considerable decline in $NO_x$ conversion across the temperature window. Among all samples, 3D-PdZ(45%)@CuZ exhibits a considerable $NO_x$ adsorption capacity (16.0 μmol $g^{-1}$) and appropriate catalytic activity (maintaining ≥95% $NO_x$ conversion within the 200–400 °C range). The 3D-PdZ(45%)@CuZ is designed to adsorb $NO_x$ at low temperatures (<170 °C) and then release $NO_x$ at 200–350 °C to react completely with $NH_3$ over the Cu-SSZ-13 shell as intended. Owing to this synergistic capacity, it is selected as a representative sample and renamed 3D-PdZ@CuZ for further discussion of its potential in PNA-SCR coupling systems.

### PNA and $NH_3$-SCR performance of integrated catalysts

To clarify the influence of the core–shell structure on catalyst performance, PNA and $NH_3$-SCR tests were performed over fresh and aged 3D-CuZ, 3D-PdZ, and 3D-PdZ@CuZ in a fixed-bed reactor. The corresponding results are depicted in Fig. 4a–f. As shown in Fig. 4a, the $NO_x$ concentration profiles show a decline upon exposure to $NO_x$, indicating the rapid adsorption of $NO_x$ on all samples at 100 °C. Immediately afterward, a $NO_x$ desorption peak appears for 3D-CuZ, illustrating that 3D-CuZ cannot trap $NO_x$ stably under the experimental conditions in the presence of $H_2O$ vapor. The NO/$NO_2$ signal profiles of 3D-CuZ indicate that there is no significant NO/$NO_2$ interconversion during the transient adsorption–desorption process (Fig. S10). Meanwhile, the 3D printed binder-only catalyst with the same structure exhibits negligible $NO_x$ adsorption, excluding weak physisorption and residence-time effects within the monolith (Fig. S11 and S12). Notably, 3D-CuZ exhibits considerable adsorption of $NO_x$ when evaluated under water-free conditions (Fig. S13). Based on the above results, it can be inferred that the adsorption sites of 3D-CuZ provide stronger interaction to $H_2O$ than $NO_x$, leading to rapid desorption of $NO_x$ in the presence of $H_2O$ (Fig. S14a). In contrast, the Pd sites in Pd-SSZ-13 retain superior capacity of $NO_x$ adsorption in the presence of $H_2O$ vapor.[39,40]

Over 3D-PdZ and 3D-PdZ@CuZ, the $NO_x$ concentration gradually approaches the starting concentrations as adsorption reaches saturation. 3D-PdZ@CuZ exhibits nearly identical $NO_x$ adsorption at 100 °C, despite having a smaller proportion of Pd-SSZ-13 compared to 3D-PdZ. A second $NO_x$ uptake occurs at around 150 °C for 3D-PdZ. As reported, adsorption of $H_2O$ at 100 °C weakens the binding of $NO_x$ to Pd sites.[41,42] With the temperature elevating, the desorption of $H_2O$ frees up partial Pd sites leading to the additional $NO_x$ uptake (Fig. S14b). On 3D-PdZ@CuZ, there is little secondary adsorption of $NO_x$. We suppose that the pre-adsorption of $H_2O$ on the Cu-SSZ-13 shell layer with a lower Si/Al ratio (4.6) effectively retards the diffusion of $H_2O$ molecules toward the Pd-SSZ-13 core, thereby extending the time window for preferential adsorption of $NO_x$ onto the active Pd sites prior to $H_2O$ breakthrough (Fig. S15 and S16). Therefore, the core–shell structured catalyst presents considerable $NO_x$ adsorption at 100 °C and the disappearance of re-adsorption peaks. Although there is only 45% loading of core materials, 3D-PdZ@CuZ (16.0 μmol $g^{-1}$) exhibits 65% adsorption capacity of 3D-PdZ (24.3 μmol $g^{-1}$) during the entire

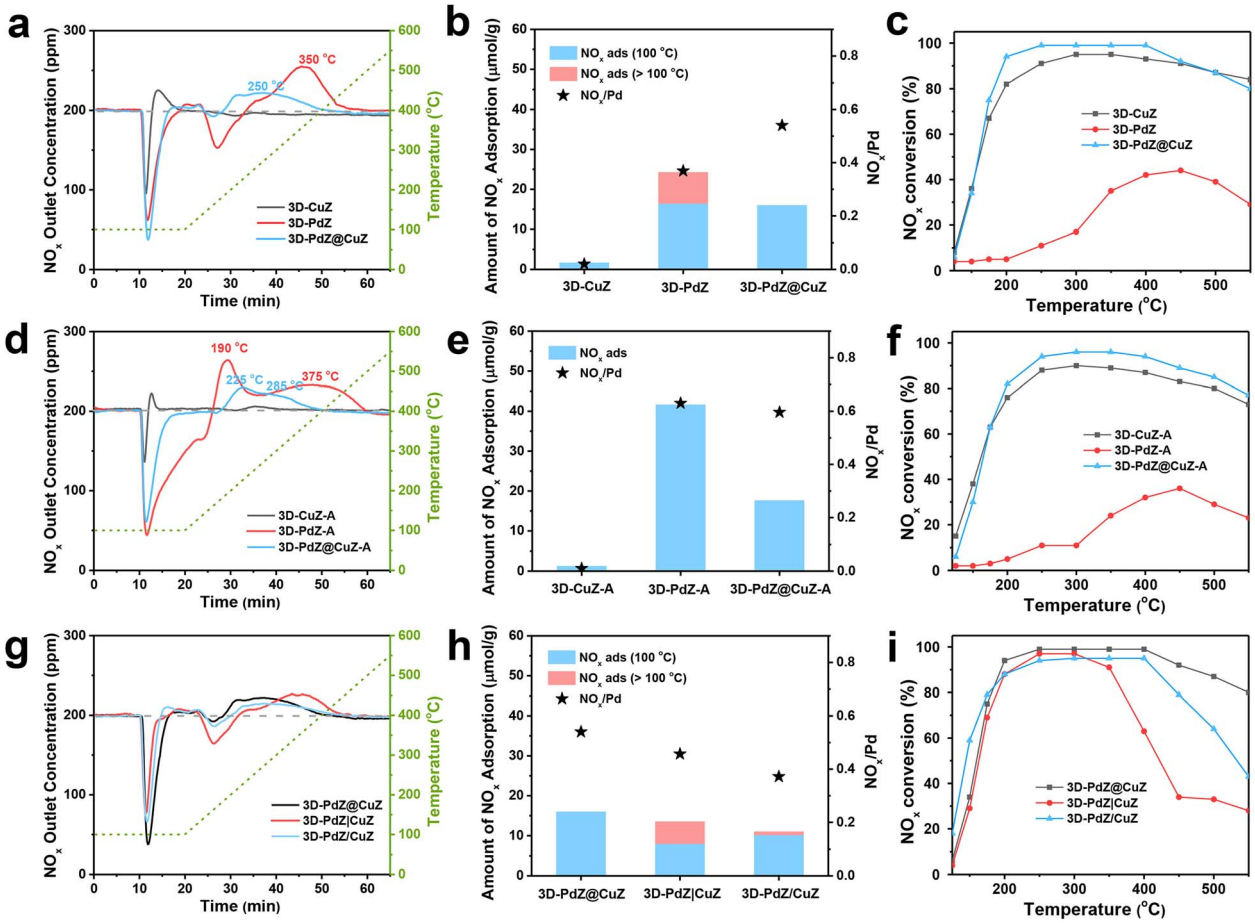


Fig. 4 PNA performance (a and d), amount of $NO_x$ adsorption and corresponding $NO_x$/Pd (b and e) of fresh (a and b) and aged (d and e) 3D-CuZ, 3D-PdZ, and 3D-PdZ@CuZ. $NH_3$-SCR performance of fresh (c) and aged (f) 3D-CuZ, 3D-PdZ, and 3D-PdZ@CuZ. PNA performance (g), amount of $NO_x$ adsorption and corresponding $NO_x$/Pd (h), and $NH_3$-SCR performance (i) of 3D-PdZ@CuZ, 3D-PdZ|CuZ, and 3D-PdZ/CuZ. (PNA reaction conditions: [NO] = 200 ppm, $[O_2]$ = 10%, $[H_2O]$ = 5%, and balanced with $N_2$. $NH_3$-SCR reaction conditions: [NO] = $[NH_3]$ = 500 ppm, $[O_2]$ = 5%, $[H_2O]$ = 5%, balanced with $N_2$, monolith sample containing 0.12 g Cu-SSZ-13, and $WHSV_{Cu\text{-}SSZ\text{-}13}$ = 100 000 $cm^3\ g^{-1}\ h^{-1}$).

storage stage (Fig. 4b). The $NO_x$/Pd ratio is also significantly improved in 3D-PdZ@CuZ (0.54) compared to 3D-PdZ (0.37), which indicates that the preparation of the core–shell structured material greatly enhances the utilization of the precious metal Pd and thus reduces the cost of PNA materials. The positive peaks above 200 ppm reflect the release of $NO_x$ when the temperatures exceed 200 °C. As shown in Fig. 4a, the desorption peaks of $NO_x$ appear at around 350 °C on 3D-PdZ and 250 °C on 3D-PdZ@CuZ, both within the appropriate temperature range of 200–350 °C for downstream $NH_3$-SCR. Notably, compared to 3D-PdZ, the lower desorption temperature of 3D-PdZ@CuZ is conducive to offer available storage sites for the next run.

To further clarify the effect of $H_2O$ on the $NO_x$ adsorption and desorption process, PNA performance of 3D-PdZ was investigated with different $H_2O$ concentrations. As shown in Fig. S17, 3D-PdZ exhibits larger adsorption capacities, smaller re-adsorption peaks, and lower desorption temperatures at lower $H_2O$ concentrations. This further supports our supposition that the Cu-SSZ-13 shell creates an environment with lower $H_2O$ concentration for the Pd-SSZ-13 layer.

The $NO_x$ adsorption–desorption curves of the samples after hydrothermal aging (10% $H_2O$, 750 °C for 16 h) are shown in Fig. 4d. The adsorption capacity of 3D-PdZ-A for $NO_x$ is greatly increased. This improvement can be ascribed to the redispersion of Pd species during hydrothermal aging, which provides more active $Pd^{2+}$/$[Pd(II)OH]^+$ sites for $NO_x$ adsorption.[40] This inference is further corroborated by the CO-DRIFTS profiles and TEM images of 3D-PdZ@CuZ and 3D-PdZ@CuZ-A (Fig. S18 and S19). However, 3D-PdZ-A exhibits two $NO_x$ desorption peaks at ~190 and ~375 °C, which are outside the desirable temperature range. In contrast, the desorption temperatures of 3D-PdZ@CuZ-A, 225 °C and 285 °C, are still favorable for $NH_3$-SCR, which can also be attributed to the weak damage on Pd-SSZ-13 from low-concentration $H_2O$ during hydrothermal aging. The adsorption capacity and $NO_x$/Pd illustrate that Pd-SSZ-13 has comparable adsorption efficiency in 3D-PdZ-A and 3D-PdZ@CuZ-A (Fig. 4e). Notably, the core–shell structured catalysts exhibit fast adsorption rates before and after hydrothermal aging, thanks to the hierarchical structure of the 3D-printed monolithic catalysts and the rapid transfer of weakly adsorbed $NO_x$ in the Cu-SSZ-13 shell.

The $NH_3$-SCR performances of fresh catalysts are depicted in Fig. 4c. 3D-PdZ exhibits poor $NH_3$-SCR activity, with a maximal $NO_x$ conversion of 45% at 450 °C. With the same Cu-SSZ-13 loading (0.12 g Cu-SSZ-13, $WHSV_{Cu\text{-}SSZ\text{-}13} = 100\,000\ cm^3\ g^{-1}\ h^{-1}$), 3D-PdZ@CuZ presents >95% $NO_x$ conversion at the temperature window from 200 to 400 °C, which is superior to that of 3D-CuZ.

This is associated with the fact that the Cu-SSZ-13 zeolites in 3D-PdZ@CuZ are mainly distributed in the ~150 μm thick shell on the outer layer of the monolith, which can be sufficiently exposed to the reaction gas. As reported, the $NH_3$-SCR reaction mainly occurs within 200 μm of the monolith surface,[43] thus 3D-PdZ@CuZ presents a higher utilization efficiency of Cu-SSZ-13 than 3D-CuZ, where Cu-SSZ-13 zeolites are distributed throughout the monolith. This is also evidenced by the comparable $NH_3$-SCR activity of 3D-CuZ and 3D-PdZ(26%)@CuZ with different loadings of Cu-SSZ-13 in Fig. 3h. It is well known that precious metals with high oxidizability usually lead to non-selective ammonia oxidation at high temperature,[29] whereas these side reactions are hardly observed in 3D-PdZ@CuZ. The design of the core–shell structured catalysts with Pd-SSZ-13 as the core and the optimal core–shell ratio greatly addresses this problem (Fig. S20). Over 3D-PdZ@CuZ with spatially confined effects, the reactants are first reacted in the Cu-SSZ-13 shell layer and most of the reductant $NH_3$ is consumed in the SCR reaction. The surplus $NH_3$ diffuses into the Pd-SSZ-13 core layer and has a chance of being oxidized to $NO_x$, which is in turn reduced to $N_2$ by $NH_3$ as it moves through the shell layer to leave the catalyst. By arranging the diffusion sequence of the gas flow over PNA and SCR catalysts, the problem of $NO_x$ escape caused by the non-selective oxidation in the PNA layer is overcome. As shown in Fig. 3h, the decrease in high-temperature activity due to non-selective ammonia oxidation is also observed on 3D-PdZ(66%)@CuZ with a thin shell layer, which further illustrates the importance of core–shell ratio controlling. As is known, hydrothermal aging generally results in a decrease in catalyst performance due to the dealumination of zeolites and aggregation of $CuO_x$. However, strikingly, 3D-PdZ@CuZ-A still presents about 8% higher conversion than 3D-CuZ-A at 200–550 °C because of the optimized distribution of Cu-SSZ-13 on the outer layer of the monolith (Fig. 4f).

$N_2O$ production, which is considered as an important aspect for SCR catalysts, is analyzed in Fig. S21. It is observed that fresh 3D-CuZ and 3D-PdZ@CuZ show minimal $N_2O$ production (<6 ppm) with excellent $NH_3$-SCR selectivity, while fresh 3D-PdZ exhibits a much higher $N_2O$ yield (20–30 ppm) at 350–550 °C due to accelerated non-selective $NH_3$ oxidation on Pd sites. After hydrothermal aging, 3D-CuZ-A and 3D-PdZ@CuZ-A maintain low $N_2O$ production (<6 ppm) below 400 °C but show increased yields (6–12 ppm) at 400–550 °C, which is attributed to the formation of additional $CuO_x$ species induced by aging that promotes non-selective $NH_3$ oxidation. This explanation is evidenced by $H_2$-TPR and XRD characterization studies of 3D-PdZ@CuZ and 3D-PdZ@CuZ-A (Fig. S22 and S23).

The influence of $SO_2$ on catalyst performance has been also investigated. Upon the addition of 50 ppm $SO_2$, the $NO_x$ adsorption amount of 3D-PdZ@CuZ increases to 20 μmol $g^{-1}$ (Fig. S24a and b). The existence of $SO_2$ seems to enhance the $NO_x$ storage in the PNA process *via* $PdSO_4$ formation and intermediate-mediated synergistic adsorption.[44] In the $NH_3$-SCR reaction (Fig. S24c), with 50 ppm $SO_2$ introduced, a significant decrease in $NO_x$ conversion is observed at temperatures below 300 °C, which is attributed to the pore blockage by $(NH_4)_2SO_4$ (decomposing at 300 °C) or $NH_4HSO_4$ (decomposing at 350 °C).[45–47] Notably, mid- and high-temperature conversions remain largely unchanged or slightly enhanced, which is attributed to sulfate species gradually decomposing and reopening the channel system of the zeolite.

To compare the catalysts with different assemblies, the layer-stacked 3D-printed catalyst with 3D-PdZ positioned in front of 3D-CuZ (3D-PdZ|CuZ) and the 3D-printed Pd-SSZ-13 and Cu-SSZ-13 mixed catalyst (3D-PdZ/CuZ) with the same PNA and SCR catalyst loading were also evaluated under the same reaction conditions (Fig. S25). The results are depicted in Fig. 4g–i. 3D-PdZ|CuZ exhibits a minimum adsorption at 100 °C and a maximum re-adsorption at 150 °C among the three samples, behaving with an adsorption–desorption profile similar to that of 3D-PdZ, as shown in Fig. 4g. Because 3D-CuZ is located downstream of 3D-PdZ in the layered 3D-PdZ|CuZ catalyst, it cannot influence the $NO_x$ adsorption and desorption process on 3D-PdZ. The dispersed Cu-SSZ-13 in 3D-PdZ/CuZ provides partial pre-adsorption of $H_2O$ and its adsorption–desorption curve is between those of 3D-PdZ@CuZ and 3D-PdZ/CuZ because the gas containing $H_2O$ diffuses randomly between Pd-SSZ-13 and Cu-SSZ-13 without a specific sequence. Notably, 3D-PdZ@CuZ provides the largest $NO_x$ adsorption capacity and the highest low-temperature adsorption percentage, indicating that the core–shell structure is superior to other combination forms in the PNA process (Fig. 4h). In the $NH_3$-SCR experiments, the $NO_x$ conversions of 3D-PdZ|CuZ and 3D-PdZ/CuZ exhibit a drastic decrease at high temperature (Fig. 4i). On 3D-PdZ|CuZ, the oxidation of $NH_3$ over Pd-SSZ-13 at high temperature leads to a shortage of reductant for the subsequent $NH_3$-SCR reaction on Cu-SSZ-13, which causes an inferior high-temperature $NH_3$-SCR performance (Fig. S26). For 3D-PdZ/CuZ, there is no spatial restriction between Pd-SSZ-13 and Cu-SSZ-13, which means $NO_x$ adsorption and desorption, ammonia oxidation, as well as $NH_3$-SCR occur independently and synchronously (Fig. S27). Thus, the $NO_x$ raised by ammonia oxidation and the $NO_x$ desorbed from Pd-SSZ-13 might leave the catalyst directly without reacting further on Cu-SSZ-13, resulting in the suppressed $NO_x$ conversion. In contrast, 3D-PdZ@CuZ still achieves 80% conversion even at 550 °C owing to the controllable diffusion sequence of the gas flow as discussed above, which suggests that the core–shell structure also presents a significant advantage in the $NH_3$-SCR reaction.

To further demonstrate the cost-effectiveness and practical viability of the core–shell catalyst, a double-coated sample (WC-PdZ@CuZ) with the same formulation was fabricated (Fig. S28). Under the PNA-SCR performance comparison, WC-PdZ@CuZ and 3D-PdZ@CuZ exhibit identical $NO_x$ adsorption capacities and $NH_3$-SCR activity, indicating that the 3D-printed core–shell catalyst does not require higher loading and cost of precious

metal or zeolite (Fig. S29). Compared to double-coated catalysts, coaxial 3D printed catalysts possess advantages of simplified fabrication of self-supporting core–shell catalysts and a tiny structure, which demonstrate a promising application prospect.

### Mimicking test of integrated catalysts

To further demonstrate the potential of this core–shell structured catalysts, a complete mimicking test of cold start and operating conditions of 3D-CuZ, 3D-PdZ@CuZ, 3D-PdZ|CuZ, and 3D-PdZ/CuZ was carried out at an equivalent WHSV of 50 000 $cm^3\ g^{-1}\ h^{-1}$ (Fig. S30). In cold start transient experiments, 200 ppm of $NO_x$ and 5% $H_2O$ were fed in a stream of 10% $O_2$ in $N_2$ at 30 °C and the temperature was rapidly increased to 200 °C in about 2 min. The temperature was then ramped up to 350 °C at 20 °C $min^{-1}$ and kept for 10 min to evaluate the behaviors of the coupled catalysts under operating conditions of vehicles. Finally, the temperature was increased to 550 °C to explore the performances of catalysts under high-temperature conditions. Note that, 500 ppm $NH_3$ was injected at about 165 °C, which is consistent with the urea decomposition temperature.

For empty tubes without the catalyst, the corresponding signals can be detected immediately after $NO_x$ and $NH_3$ are introduced, as shown in Fig. S31. Over 3D-CuZ, a large amount of $NO_x$ is released during the cold start stage (Fig. 5a). As the temperature increases, the $NO_x$ concentration gradually decreases after the addition of $NH_3$ until it is completely reacted at 300 °C. 3D-CuZ exhibits great removal performance of $NO_x$ at medium and high temperatures, which is attributed to the $NH_3$-SCR activity of Cu-SSZ-13.

As depicted in Fig. 5b, $NO_x$ concentration is remarkably reduced during the cold-start stage on 3D-PdZ@CuZ. NO and $NO_2$ concentrations gradually increase up to 65 ppm and 18 ppm with Pd-SSZ-13 adsorption saturated. As the temperature increases to the active window for an effective $NH_3$-SCR reaction, $NO_x$ is entirely removed throughout the medium and high temperature ranges. Over 3D-PdZ|CuZ (Fig. 5c) and 3D-PdZ/CuZ (Fig. 5d), the $NO_x$ removal efficiencies are also excellent in the mid-temperature stage. However, there is increased $NO_x$ overflow at low and high temperature stages because of the limited $NO_x$ adsorption capacity and the non-selective oxidation of $NH_3$, particularly on 3D-PdZ|CuZ. For the entire mimicking process, 3D-PdZ@CuZ displays the best overall $NO_x$ removal efficiency up to 96%, compared to 3D-CuZ (90%), 3D-PdZ|CuZ (75%), and 3D-PdZ/CuZ (89%), demonstrating the significant advantages of coaxial 3D-printed core–shell composite structures in addressing cold-start $NO_x$ emissions. Besides, 3D-PdZ@CuZ-A also maintains an outstanding $NO_x$ removal efficiency (92%) after hydrothermal aging, which indicates the long-term stability of the core–shell integrated catalyst (Fig. S32).

A series of comparative tests were conducted to further clarify the contributions of Pd-SSZ-13 and Cu-SSZ-13 in the removal of $NO_x$. $NO_x$ and $NH_3$ were pre-stabilized in the bypass line to perform the mimicking test. After switching the gas mixture to the reaction line, the rapid decrease in $NO_x$ concentration can be clearly observed in Fig. S33 and S34, which directly demonstrates the adsorption process over Pd-SSZ-13 compared to Fig. 5b. The adsorption–desorption profile of $NO_x$ was also carried out in the presence of $NH_3$ (Fig. S35). In addition to the adsorption peak of Pd-SSZ-13 at 100 °C, it is easily observed that the $NO_x$ concentration gradually tends to 0 as the temperature increases. This suggests that $NO_x$ reacts with $NH_3$ on Cu-SSZ-13 and the $NO_x$ stored in Pd-SSZ-13 is consumed by the $NH_3$-SCR reaction after desorption. The above discussion demonstrates the successful implementation of the adsorption and catalysis integrated core–shell structure, which not only exhibits excellent $NO_x$ removal activity but also avoids the introduction of costly additional components.

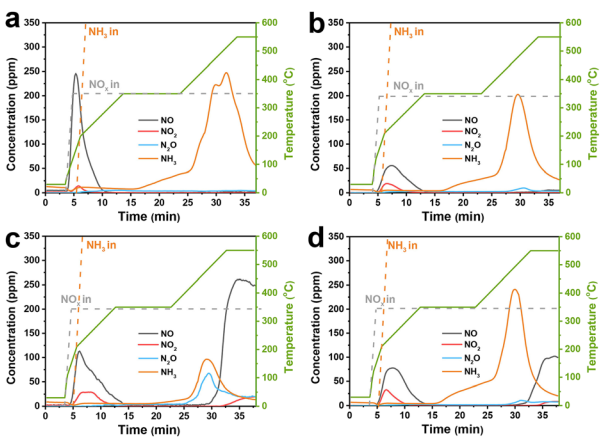


Fig. 5 Mimicking test on 3D-CuZ (a), 3D-PdZ@CuZ (b), 3D-PdZ|CuZ (c), and 3D-PdZ/CuZ (d). (Reaction conditions: [NO] = 200 ppm, [$NH_3$] = 500 ppm, [$O_2$] = 10%, [$H_2O$] = 5%, balanced with $N_2$, 0.24 g monolith, and WHSV = 50 000 $cm^3\ g^{-1}\ h^{-1}$).

## Conclusions

In summary, we have successfully fabricated 3D-PdZ@CuZ core–shell structured catalysts *via* coaxial 3D printing for integrated $NO_x$ capture and catalysis to efficiently remove $NO_x$ from the cold start stage. Over this integrated catalyst, $NO_x$ could be trapped in Pd-SSZ-13 at low temperature (<170 °C), and released from Pd-SSZ-13 to react with $NH_3$ on Cu-SSZ-13 at 200–350 °C, achieving a boosted synergistic effect of PNA and SCR during the cold start. The outstanding behavior of the coupled catalyst is mainly attributed to the unique macroscopic core–shell structure with spatially confined effects. During the adsorption process, the Cu-SSZ-13 shell can pre-adsorb $H_2O$, resulting in low $H_2O$ content in the Pd-SSZ-13 layer, hence 3D-PdZ@CuZ exhibits a higher adsorption capacity ($NO_x$/Pd = 0.54), optimised desorption temperature (~250 °C), and greater anti-aging properties compared to 3D-PdZ. On the other hand, the $NH_3$-SCR occurred in the zeolite shell could effectively isolate the Pd-SSZ-13 core from $NH_3$ and restrain the side reaction of ammonia oxidation, contributing to the excellent $NH_3$-SCR activity of 3D-PdZ@CuZ. Additionally, the core/shell ratio plays an important role in balancing the adsorption and catalytic properties. By controlling the composition and distribution of the active components in the core–shell structure, 3D-PdZ@CuZ exhibits superior $NO_x$ removal efficiency (96%) in the

mimicking test of the cold start and operating conditions, outperforming 3D-CuZ (90%), 3D-PdZ|CuZ (75%), and 3D-PdZ/Cu (89%). This work provides a facile strategy for coupling the PNA process into existing exhaust treatment systems to overcome the cold start challenge of $NO_x$ elimination from diesel vehicles by coaxial 3D printing of integrated PNA-SCR core–shell structured catalysts.

## Author contributions

Yingzhen Wei: conceptualization, formal analysis, and writing – original draft preparation. Jingyi Feng: investigation, formal analysis, and writing – original draft preparation. Dan Li: formal analysis. Youji Qi: data curation. Mengyang Chen: visualization. Shuang Wang: manuscript revision. Jinfeng Han: validation. Jihong Yu: conceptualization, project administration, writing – review & editing, and funding acquisition.

## Conflicts of interest

There is no conflict of interest to report.

## Data availability

All data associated with this article have been included in the main text and supplementary information (SI). Supplementary information is available. See DOI: https://doi.org/10.1039/d5sc08988c.

## Acknowledgements

The authors thank the National Natural Science Foundation of China (Grant No. 22288101, 22105093, and 22301209), the National Key Research and Development Program of China (Grant No. 2021YFA1501202), the '111 Center' (B17020), and the Natural Science Foundation of Jilin Province (Grant No. SKL202502014JC) for supporting this work.

## Notes and references

1 Y. Wu, T. Andana, Y. Wang, Y. Chen, E. D. Walter, M. H. Engelhard, K. G. Rappé, Y. Wang, F. Gao, U. Menon, R. Daya, D. Trandal, H. An, Y. Zha and K. Kamasamudram, *Appl. Catal., B*, 2022, **318**, 121807.
2 J. Becher, D. F. Sanchez, D. E. Doronkin, D. Zengel, D. M. Meira, S. Pascarelli, J.-D. Grunwaldt and T. L. Sheppard, *Nat. Catal.*, 2020, **4**, 46–53.
3 Y. Bai, D. Hao, Y. Wei, J. Han, D. Li, M. Chen and J. Yu, *Mater. Chem. Front.*, 2024, **8**, 2142–2148.
4 T. Zhang, F. Qiu and J. Li, *Appl. Catal., B*, 2016, **195**, 48–58.
5 Q. Lin, C. Lin, J. Liu, S. Liu, H. Xu, Y. Chen and Y. Dan, *Chem. Res. Chin. Univ.*, 2020, **36**, 1249–1254.
6 M. Chen, W. Zhao, Y. Wei, J. Han, J. Li, C. Sun, D. Mei and J. Yu, *Nano Res.*, 2023, **16**, 12126–12133.
7 Y. Wang, J. Han, M. Chen, W. Lv, P. Meng, W. Gao, X. Meng, W. Fan, J. Xu, W. Yan and J. Yu, *Angew. Chem., Int. Ed.*, 2023, **62**, e202306174.
8 M. Chen, J. Li, W. Xue, S. Wang, J. Han, Y. Wei, D. Mei, Y. Li and J. Yu, *J. Am. Chem. Soc.*, 2022, **144**, 12816–12824.
9 Y. Shan, G. He, J. Du, Y. Sun, Z. Liu, Y. Fu, F. Liu, X. Shi, Y. Yu and H. He, *Nat. Commun.*, 2022, **13**, 4606.
10 Y. Shan, J. Du, Y. Zhang, W. Shan, X. Shi, Y. Yu, R. Zhang, X. Meng, F. S. Xiao and H. He, *Natl. Sci. Rev.*, 2021, **8**, nwab010.
11 Y. Wei, M. Chen, X. Ren, Q. Wang, J. Han, W. Wu, X. Yang, S. Wang and J. Yu, *CCS Chem.*, 2022, **4**, 1708–1719.
12 E. Bello, V. J. Margarit, E. M. Gallego, F. Schuetze, C. Hengst, A. Corma and M. Moliner, *Microporous Mesoporous Mater.*, 2020, **302**, 110222.
13 H. Geerts-Claes, S. Smet, C. Hengst, F.-W. Schuetze, E. Verheyen, M. Minjauw, C. Detavernier, S. Pulinthanathu Sree and J. Martens, *J. Phys. Chem. C*, 2023, **127**, 7119–7130.
14 K. Khivantsev, N. R. Jaegers, L. Kovarik, J. Z. Hu, F. Gao, Y. Wang and J. Szanyi, *Emiss. Control Sci. Technol.*, 2019, **6**, 126–138.
15 D. Li, Q. Ding, D. Hao, J. Han, G. Yang, L. Pang, Y. Guo, J. Yu and T. Li, *Environ. Sci. Technol.*, 2023, **57**, 19956–19964.
16 M. Moliner and A. Corma, *React. Chem. Eng.*, 2019, **4**, 223–234.
17 H. Zhao, X. Chen, A. Bhat, Y. Li and J. W. Schwank, *Appl. Catal., B*, 2021, **286**, 119874.
18 K. Khivantsev, N. R. Jaegers, L. Kovarik, S. Prodinger, M. A. Derewinski, Y. Wang, F. Gao and J. Szanyi, *Appl. Catal., A*, 2019, **569**, 141–148.
19 D. Li, Q. Ding, Y. Meng, Y. Guo, L. Pang and T. Li, *Sep. Purif. Technol.*, 2023, **322**, 124344.
20 K. Khivantsev, N. R. Jaegers, L. Kovarik, J. C. Hanson, F. Tao, Y. Tang, X. Zhang, I. Z. Koleva, H. A. Aleksandrov, G. N. Vayssilov, Y. Wang, F. Gao and J. Szanyi, *Angew. Chem., Int. Ed.*, 2018, **57**, 16672–16677.
21 D. Li, Y. Meng, D. Hao, Q. Ding, L. Pang, G. Yang, Y. Guo, J. Yu and T. Li, *Chem. Eng. J.*, 2022, **446**, 136779.
22 Y. Shan, Y. Sun, Y. Li, X. Shi, W. Shan, Y. Yu and H. He, *Top. Catal.*, 2020, **63**, 944–953.
23 M. E. Azzoni, F. S. Franchi, N. Usberti, N. D. Nasello, L. Castoldi, I. Nova and E. Tronconi, *Appl. Catal., B*, 2022, **315**, 121544.
24 F. Gramigni, T. Selleri, I. Nova, E. Tronconi, S. Dieterich, M. Weibel and V. Schmeisser, *Top. Catal.*, 2019, **62**, 3–9.
25 T. Selleri, F. Gramigni, I. Nova, E. Tronconi, S. Dieterich, M. Weibel and V. Schmeisser, *Catal. Sci. Technol.*, 2018, **8**, 2467–2476.
26 A. Wang, K. Xie, A. Kumar, K. Kamasamudram and L. Olsson, *Catal. Today*, 2021, **360**, 356–366.
27 S. Lawson, X. Li, H. Thakkar, A. A. Rownaghi and F. Rezaei, *Chem. Rev.*, 2021, **121**, 6246–6291.
28 X. Wen, B. Zhang, W. Wang, F. Ye, S. Yue, H. Guo, G. Gao, Y. Zhao, Q. Fang, C. Nguyen, X. Zhang, J. Bao, J. T. Robinson, P. M. Ajayan and J. Lou, *Nat. Mater.*, 2021, **20**, 1506–1511.
29 L. Long, R. Pei, Y. Liu, X. Rao, Y. Wang, S.-f. Zhou and G. Zhan, *J. Hazard. Mater.*, 2022, **423**, 126983.
30 A. K. Mohammed, S. Usgaonkar, F. Kanheerampockil, S. Karak, A. Halder, M. Tharkar, M. Addicoat,

T. G. Ajithkumar and R. Banerjee, *J. Am. Chem. Soc.*, 2020, **142**, 8252–8261.
31 C. Huo, S. Wu, R. Zhang, Z. Wu, X. Tian, L. Tan, K. Li, Y. Yang, B. Wang, Z. Hu, L. Wu and D. Li, *Adv. Mater.*, 2025, **37**, 2508078.
32 C. Y. Chaparro-Garnica, E. Bailón-García, D. Lozano-Castelló and A. Bueno-López, *Catal. Sci. Technol.*, 2021, **11**, 6490–6497.
33 Y. Wang, S. Lin, M. Li, C. Zhu, H. Yang, P. Dong, M. Lu, W. Wang, J. Cao, Q. Liu, X. Feng, H. Hu, N. Tsubaki and M. Wu, *Appl. Catal., B*, 2024, **340**, 123211.
34 Y. Wu, J. He, W. Huang, W. Chen, S. Zhou, X. She, W. Zhu, F. Huang, H. Li and H. Xu, *Fuel*, 2023, **332**, 126021.
35 R. Wang, Y. Gong, P. Wang, W. He, Y. Song, M. Xin, Q. Jiang, Y. Sha, T. Cao, H. Song and W. Lin, *J. Mater. Chem. A*, 2023, **11**, 13945–13955.
36 S. Wang, P. Bai, M. Sun, W. Liu, D. Li, W. Wu, W. Yan, J. Shang and J. Yu, *Adv. Sci.*, 2019, **6**, 1901317.
37 S. Wang, P. Bai, Y. Wei, W. Liu, X. Ren, J. Bai, Z. Lu, W. Yan and J. Yu, *ACS Appl. Mater. Interfaces*, 2019, **11**, 38955–38963.
38 Y. Wei, S. Wang, M. Chen, J. Han, G. Yang, Q. Wang, J. Di, H. Li, W. Wu and J. Yu, *Adv. Mater.*, 2024, **36**, 2302912.
39 Y. Li, D. Chen, X. Xu, X. Wang, R. Kang, M. Fu, Y. Guo, P. Chen, Y. Li and D. Ye, *Environ. Sci. Technol.*, 2023, **57**, 3467–3485.
40 Y. Wang, X. Shi, Z. Liu, Y. Shan, W. Shi, Y. Yu and H. He, *Appl. Catal., B*, 2023, **324**, 122254.
41 D. Li, G. Yang, M. Chen, L. Pang, Y. Guo, J. Yu and T. Li, *Appl. Catal., B*, 2022, **309**, 121266.
42 A. Gupta, S. B. Kang and M. P. Harold, *Catal. Today*, 2021, **360**, 411–425.
43 C. Zheng, L. Xiao, R. Qu, S. Liu, Q. Xin, P. Ji, H. Song, W. Wu and X. Gao, *Chem. Eng. J.*, 2019, **361**, 874–884.
44 D. Yao, P. H. Ho, J. C. Wurzenberger, T. Glatz, W. Di, R. F. Ilmasani, D. Creaser and L. Olsson, *Chem. Eng. J.*, 2024, **487**, 150406.
45 Y. Wang, X. Ren, K. Li, Y. Shao, Y. Zhou, M. Zhao, C. Liu, Y. Liu, X. Liu, A. Dong, H. Wu, M. Wang, L. Meng, W. Zhang, Z. Li and Q. Liu, *Fuel*, 2025, **392**, 134818.
46 Y. Jangjou, Q. Do, Y. Gu, L.-G. Lim, H. Sun, D. Wang, A. Kumar, J. Li, L. C. Grabow and W. S. Epling, *ACS Catal.*, 2018, **8**, 1325–1337.
47 R. Yu, Z. Zhao, S. Huang and W. Zhang, *Appl. Catal., B*, 2020, **269**, 118825.